AGRICULTURAL MONITORING BY HIGH FREQUENCY AND HIGH RESOLUTION MULTIPLE SATELLITES AND ITS APPLICATIONS TO HARVESTING DETECTION

Takuto Shimode[1], Akira Iwasaki[1] and Yoshio Inoue[2]
[1]Department of Aeronautics and Astronautics, The University of Tokyo, 113-8656 Tokyo, Japan,
[2]Department of Biological and Environmental Engineering, The University of Tokyo, 113-8656 Tokyo, Japan,
E-mail: shimode-takuto909@g.ecc.u-tokyo.ac.jp, aiwasaki2@g.ecc.u-tokyo.ac.jp
yoshio.inoue@mail.u-tokyo.ac.jp

KEY WORDS: multi-satellite, harvest, NDVI, time-series, fusion

ABSTRACT: While the use of satellite imagery for various time series analysis has been increasing in recent years, it has been difficult to perform such analysis with high accuracy because of the data missing caused by cloud contamination and the limited frequency of single satellite observation. In recent years, data from high temporal and spatial resolution satellites, such as Planet Labs Dove and VENμS, have become available. In this work, we pre-processed these two satellite images, correcting for differences in resolution and geolocation, and removing clouds, so that they can be used in the integrated manner. Then, using these integrated data from multiple satellite observation, we truck the behavior of each reflectance and vegetation indexes and detect the harvest date

The first analysis trucked the seasonal behavior of each reflectance and NDVI. It was found that the data from both Planet Labs Dove and VENμS satellites could be treated equivalently in tracking NDVI. As a result, periodic seasonal changes of NDVI were captured over three years. In addition, by using NDVI as a relative index instead of directly using a single band reflectance, it was confirmed that it was possible to reduce the noise that may have originated from the instrumental characteristics between different satellites and the acquisition time as well as atmospheric correction error.

Second, we smoothed vegetation indexes, NDVI and EVI2, with Savitzky-Golay filter and compared them with each other. As a result, it was confirmed that the overall variance of EVI2 was smaller than that of NDVI and that EVI2 was more resistant to outliers. Finally, the harvest date was actually detected for the 200 correct data points using a method based on the threshold of time series NDVI. we detected harvesting with a mean absolute difference of 5.4 days, and the overall harvesting detection rate was 71.5%.

1. INTRODUCTION

There have been many studies on time series analysis using satellite images. Landsat, with 16-day revisit cycle and 30m resolution, has been widely used for land cover monitoring and land-cover change detection due to its ability to analyze a wide range of areas over a long period of time. For example, confirmation of long-term burning and recovery in forests and monitoring of land disturbance have been carried out (Suming, et al., 2017) (Hasi, et al., 2020) (Zhe, et al., 2020). On the other hand, land mapping using sentinel-2, with 10-day revisit cycle and 10~60m resolution, is also common (Grabska, et al., 2019). However, long observation cycles of these satellites and frequent cloud contamination limit their application for detecting rapid changes in the area. Meanwhile, low-resolution, high-frequency satellites, such as Moderate Resolution Imaging Spectroradiometer (MODIS), with 1-day revisit cycle and 250~1000m resolution, has been used for more abrupt and short period change detection. The prediction of yield and harvest date from time series data using MODIS has been studied (Petersen, 2018). However, due to the limitations of its spatial resolution, most of the analysis is limited to a broad land scale, and not much analysis has been done on the individual field of farmland. There is currently a trade-off between the resolution of these images and the frequency of shooting, so it is difficult to acquire remotely sensed data with both high spatial resolution and frequent coverage.

On the other hand, in recent years, there has been a growing demand for continuous monitoring of crop growth and land use. Satellite monitoring can not only provide farmers with effective information for efficient farm management, but also has great administrative value in that it can mechanically perform extensive land management based on images. The importance of satellite monitoring is high in a country like Japan, where the population is declining and aging, making it necessary to save manpower.

As a solution to the shortcomings of existing optical satellites, as pointed out earlier, some studies have been conducted using Synthetic Aperture Radar (SAR) such as Sentinel-1, which is not affected by clouds and has a

relatively high imaging frequency (Shang, et al., 2020) (Sebastián, et al., 2021). At the same time, the generation and utilization of time series data by fusing multiple satellite images of different resolutions and acquisition frequencies, such as Landsat and MODIS, have also been studied for many years (Feng, et al., 2006) (Rao, et al., 2015). Some have investigated the impact of fused data on the ability to explain spatial and temporal variability in crop fields (Gao, et al., 2018).

In recent years, more frequent and higher resolution satellite images have become available. Dove and VENμS are two examples of high frequency and spatial resolution. Their revisit time is one or two days and the resolution is less than 10 meters. By using these data, it is possible to detect the changes originating from the cropping and harvesting of land in each farm field unit with an accuracy of one or two days. Gao et al. used VENuS satellite data for Detecting cover crop end-of-season and detected its harvesting with high accuracy (Gao, et al., 2020). However, analysis of these new satellite imagery is still rare and has several problems, such as clouds and atmospheric correction, which have not been systematically solved. Therefore, research so far has been limited to the fusion of VENuS and existing satellites, Sentinel-1 (Manivasagam, et al.,2019). Especially, VENuS researches to fuse these new high temporal and spatial resolution satellite images and analyze them in time-series are limited for now. By integrating multiple satellite data, we can obtain more time-dense information, which enables us to conduct more accurate analysis. Some research evaluated the impact of the number of resampled dates on a NDVI time series using VENμS satellite (Carlos, et al., 2021).

In this work, we used Dove and VENμS satellite imagery and first built an infrastructure that can handle multiple satellite images in an integrated manner. For this purpose, adjustments in resolution, correction of misalignment, and removal of clouds were carried out. Then, we used them to track time series of reflectance and a vegetation index at farmland area and assessed them. Finally, we smoothed NDVI and EVI2 using Savitzky-Golay filter and tried to detect harvesting event in the target area.

2. DATASET AND DATA-CUBE GENERATION

2.1. Dataset

In this work, Planet Labs Dove satellite and VENμS satellite imagery was used for time-series analysis of the multiple satellites. Dove, a 3U CubeSat remote sensing satellite, forms a constellation composed of more than 100 satellites. The images were provided by Planet Labs. Its revisit time is less than one day and it has four bands, including R, G, B, and NIR. VENμS is a satellite which is jointly developed and operated by ISA (Israel Space Agency) and CNES (Centre National dEtudes SpatialesEtudes Spatiales). The observation frequency is two days and the number of bands is 12. The detail specifications of each satellite are shown in Table 1. Four spectral bands of VENuS (bands 3, 4, 5, 11), which overlap with the spectral bands of Dove, are used in this work.

For each dataset, radiance calibration, ortho correction and the atmospheric correction was conducted to convert the DN value to Land Surface Reflectance (LSR). For the atmospheric correction, we used the atmospherically corrected Level 2 product as the VENuS data set, and the QUAC (Quick Atmospheric Correction) method was used to correct the Dove satellite images. Imagery of two satellites was prepared for 3 years from 2018 to 2020. Since each dataset has different resolution and acquisition time, some preprocess is needed to integrate and analyze the multi satellite images.

Table. 1 Specifications of Satellites

	Dove	VENuS
Resolution	3 m	5 m
Revisit time	<1 day	2 days
Bands	4	12
Satellites	110+	1
Blue	B1(445 – 515nm)	B3(470 – 510nm)
Green	B2(500 – 590nm)	B4(535 – 575nm)
Red	B3(590 – 670nm)	B5(614 – 662nm)
NIR	B4(780 – 860nm)	B11(845 – 885nm)
Acquisition time	9:30-11:30 am	10:30 am

2.2 Study Area

The study area covers Minamisoma City, Fukushima, Japan. The site is as shown in Fig. 1. The yellow circle indicates the location of farmland, which was analyzed later in the time series tracking. The areas surrounded in red are the areas where the harvest date was provided as ground reference data used in later harvesting detection. The data with the harvest date recorded for each farm field was received from two agricultural corporations in the target area. One data set consisted of 76 data points in 2019 and 104 data points in 2020, while the other data set consisted of 20 data points in 2020.

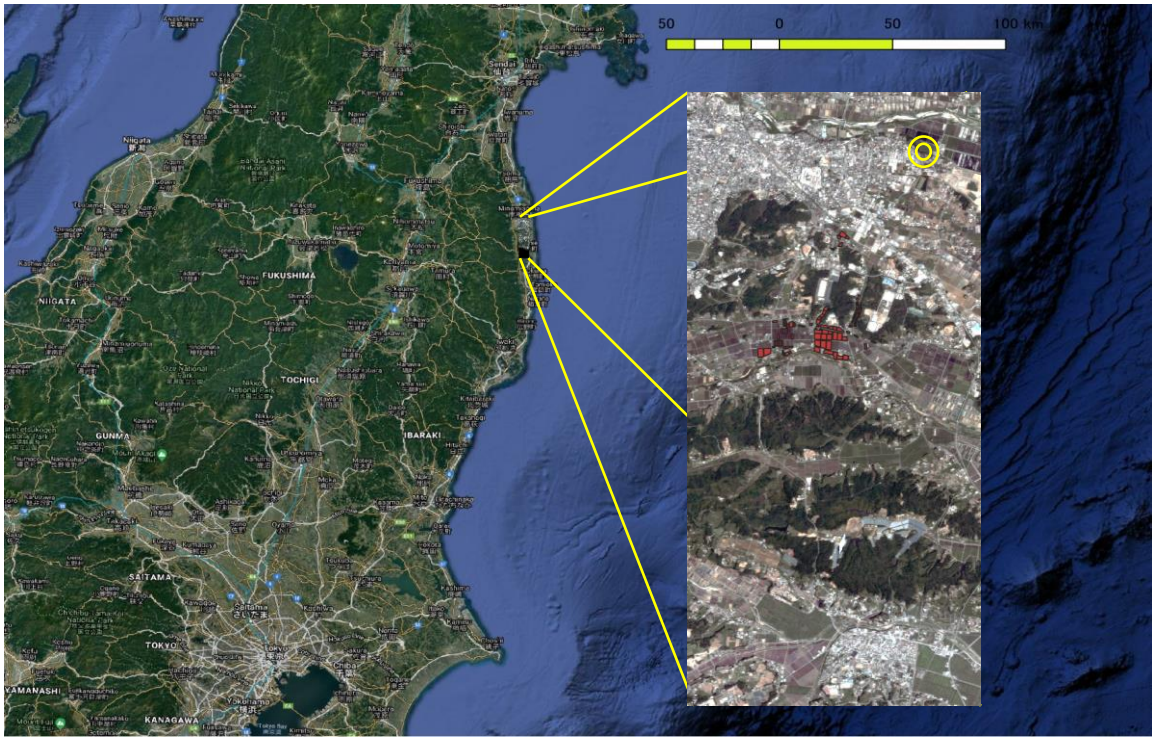

Fig. 1 The Studying Area

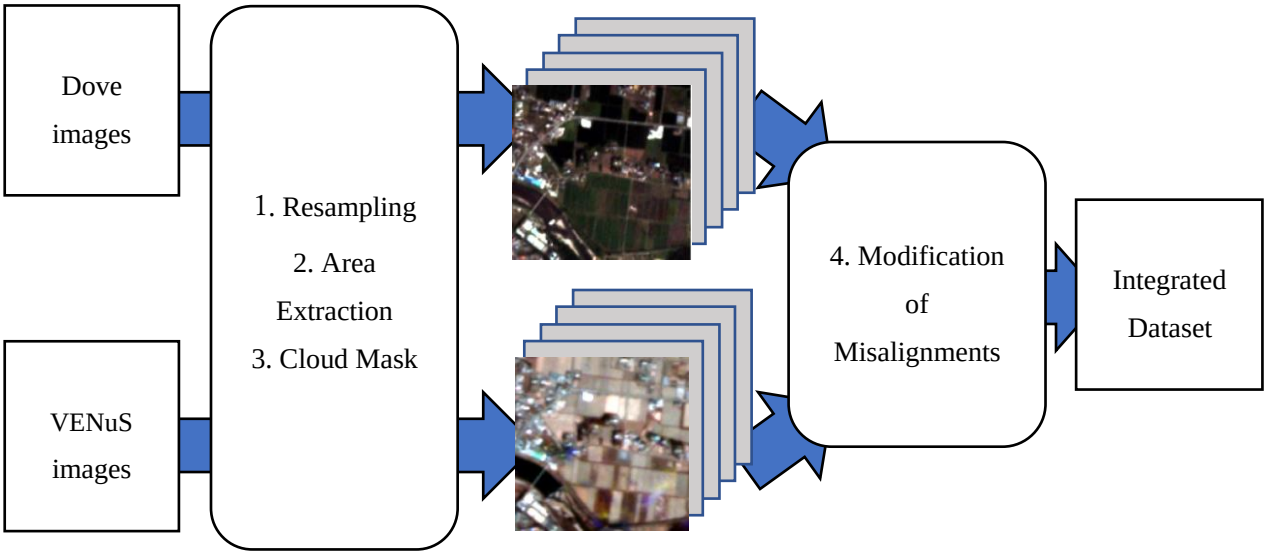

Fig. 2 Flowchart of image processing for multi-satellite integration.

2.3. Data-cube Generation

The following pre-processing is required for the integrated analysis of the two satellite images. The process below is applied to each farmland to be analyzed and forms a data set.

Fig. 2 shows the flowchart for integrating Dove and VENµS imagery. First, since the resolution of both satellites was different, as shown in Table 1, the Dove satellites images were down-sampled to match the VENµS image resolution of 5 meters using bi-linear resampling method. Then the extraction of the target area was conducted.

Third, in order to remove cloudy images, we used the cloud mask provided by the Level2 product for VENµS satellite images. On the other hand, for Dove satellite images, cloud images were detected and removed using a method based on threshold and correlation coefficient. This method is to calculate the correlation coefficients of extracted images, using a cloud-free image as a reference. And then, images with correlation coefficients lower than 0.2 were removed as containing clouds.

Fourth, even though each image has the same geographic coordinate system (WGS84), when the images are actually compared with each other based on the coordinate information, a slight misalignment was visually confirmed. To solve this problem, a clear image with few clouds was selected as the reference image among the VENµS satellite images, and the misalignment of both Dove and VENµS satellite images with respect to that reference image was obtained using phase correlation method. Then the misalignment was corrected by shifting all images in parallel according to the calculated result. After these 4 steps, a time-series data-cube of the target area where the both satellites' data were fused together was created.

3. METHODS

3.1. NDVI and EVI2

Normalized Difference Vegetation Index (NDVI) is a vegetation index which is calculated as formula (Quan, et al., 2005).

$$NDVI = \frac{NIR - VIS}{NIR + VIS} \tag{1}$$

VIS and NIR stand for the spectral reflectance of the visible band (red band) and near-infrared band, respectively (Compton, 1979). The value of NDVI takes the range from -1 to 1. When the vegetation is high, the reflectance of VIS is low and the reflectance of NIR is high. As a result, a larger NDVI value means higher vegetation.

2-band enhanced vegetation index (EVI2) is also a vegetation index calculated as formula (2) (Zhangyan, et al, 2008).

$$EVI2 = 2.5 * \frac{(NIR - RED)}{(NIR + 2.4 * RED + 1.0)} \tag{2}$$

RED and NIR represent spectral reflectance of the red band and near-infrared band, respectively.
Unlike normal EVI, it does not require the reflectance of the blue band, and EVI2 has several advantages over NDVI including the ability to resolve leaf area index (LAI) differences for vegetation with different background soil reflectance (Adrian, et al, 2009).

3.2. Phase Only Correlation

The phase only correlation match the 2 input images using the phase spectrum after the Fourier transform of input images (Koichi, et al., 2008). First the two input images are Fourier transformed and the amplitude spectrum is replaced with a fixed value to make an image with only phase information.

$$F_1(u,v) = \sum_{m=0}^{M-1}\sum_{n=0}^{N-1} f_1(m,n)e^{-j2\pi\left(\frac{mu}{M}+\frac{nv}{N}\right)} \tag{3}$$

$$= A(u,v)e^{j\theta(u,v)} \tag{4}$$

$$F_2(u,v) = \sum_{m=0}^{M-1}\sum_{n=0}^{N-1} f_2(m,n)e^{-j2\pi\left(\frac{mu}{M}+\frac{nv}{N}\right)} \quad (5)$$

$$= B(u,v)e^{j\emptyset(u,v)} \quad (6)$$

$$F_1'(u,v) = e^{j\theta(u,v)} \quad (7)$$

$$F_2'(u,v) = e^{j\emptyset(u,v)} \quad (8)$$

After that, one phase image is multiplied by the complex conjugate of the other phase image to make a composite image.

$$H_{12}(u,v) = F_1'(u,v)(F_2'(u,v))^* \quad (9)$$

$$= e^{j(\theta-\emptyset)} \quad (10)$$

Then the inverse Fourier transform is applied to it to obtain the correlation intensity image.

$$G_{12}(r,s) = \sum_{u=0}^{M-1}\sum_{v=0}^{N-1}(H_{12}(u,v))e^{j2\pi\left(\frac{ur}{M}+\frac{vs}{N}\right)} \quad (11)$$

$$= \sum_{u=0}^{M-1}\sum_{v=0}^{N-1}(e^{j(\theta-\emptyset)})e^{j2\pi\left(\frac{ur}{M}+\frac{vs}{N}\right)} \quad (12)$$

By looking at the position of the peak of the correlation intensity image, the amount of misalignment between the two images can be determined.

3.3. The Savitzky-Golay Filter

The Savitzky-Golay filter (SG-filter) is one of the digital filters used to smooth out the consecutive values (a spectrum) and reduce the effect of noises (Savitzky, et al., 1964). In the process of the convolution, this filter approximates the window frame data with a polynomial, perform fitting by the method of linear least squares, and then use the calculated value of the polynomial as the value after smoothing. This filter can be applied to any consecutive data when the points of the data are at a fixed and uniform interval, and the curves formed by graphing the points must be continuous and somewhat smooth.
In this work, we truck the time series change of vegetation indexes and they satisfy these conditions.
The general equation of the simplified least-squares convolution for NDVI time-series smoothing can be given as follows:

$$Y_j^* = \frac{\sum_{i=-m}^{i=m} C_i Y_{j+i}}{N}, \quad (13)$$

where *Y* is the original NDVI value, *Y** is the resultant NDVI value, *Ci* is the coefficient for the ith NDVI value of the filter (smoothing window), and *N* is the number of convoluting integers and is equal to the smoothing window size (2*m* + 1). The index *j* is the running index of the original ordinate data table. The smoothing array (filter size) consists of 2*m* + 1 points, where m is the half-width of the smoothing window. There are two parameters for the filter, *m*, which is half the length of the smooth window, and *d*, the degree of the smoothing polynomial.

3.4. Exponential Moving Average

An exponential moving average (EMA) is a type of moving average (MA) that places a greater weight and significance on the most recent data points. An exponentially weighted moving average reacts more significantly to recent value changes (Seng, 2013). The EMA for a time series can be calculated recursively

$$EMA_1 = Y_1 \tag{13}$$

$$for\ t > 1, EMA_t = \alpha * Y_t + (1 - \alpha) * EMA_{t-1}, \tag{14}$$

where "Yt" is the value at time period t, "EMAt" is the value of EMA at time period t, and "α" represents the degree of weighting decrease, a constant smoothing factor between 0 and 1. Commonly, α is calculated using the formula

$$\alpha = \frac{2}{N + 1} \tag{15}$$

Therefore, the smaller N is, the more sensitive the EMA value is to the original value.

4. RESULTS AND DISCUSSION

We first tracked the time-series changes of reflectance on the pixels of the target farmland, which is indicated by the circle in Fig. 1. In order to reduce the influence of noises, the average value of 3×3 pixels around the target pixel were used as the representative value.

4.1. The Trucking of Time-Series Reflectance

Fig. 3 shows a time-series plot of the reflectance of R, G, B, and NIR at a farmland pixel. The orange dots are from the VENμS satellite, whereas the blue dots are from the Dove satellites. Each reflectance shows a similar trend in R, G, and B reflectance, which distributed between 0 and 0.2 throughout the year, and there is no significant difference between the Dove and VENμS satellite-derived data. In contrast, the NIR reflectance of both satellites show an overall trend of increasing from March to September and decreasing values from September to the following March. Furthermore, the NIR reflectance obtained by Dove shows a larger variance than the NIR reflectance obtained by the VENμS satellites. This is thought to be due to the differences in sensor characteristics and imaging wavelengths of the two satellites, as well as the effects of the sun illumination angle due to the observation geometry.

Fig. 3 Time-series plot of R, G, B, and NIR bands for Farmland pixels

4.2. The Trucking of Time-Series NDVI

Next, we evaluated NDVI, an index calculated from two spectral bands. As shown in Fig. 4(a), NDVI in farmland tends to increase from March to September and decrease from September to the following March throughout the entire period. Although the NDVI values are significantly lower than usual only in around May 2020, both Dove and VENuS satellite-derived plots show similar values for the entire three years of data, indicating that the effect of the difference in NIR dispersion confirmed in 4.1 has been reduced. This may be attributed to the suppression of reflectance variation by taking the ratio between the bands. With proper pre-processing, it can be said that NDVI of two different satellites can be equally evaluated and used for analysis.

To perform time series analysis on the integrated NDVI, the entire data was smoothed to take missing data into account. For the smoothing method, we used the SG filter, which was found to be effective after a comparative study of the SG filter and other smoothing methods for NDVI (Cai, et al., 2017). Also, for the SG filter, we used an algorithm that was modified to be more effective in tracking NDVI (Jin, et al., 2004). Fig. 4(b) shows the time series of NDVI after linear interpolation and SG-filter, at the same location as before. It shows that the negative NDVI outlier observed around October 2020 has been mitigated and the plot is less sensitive to extremes.

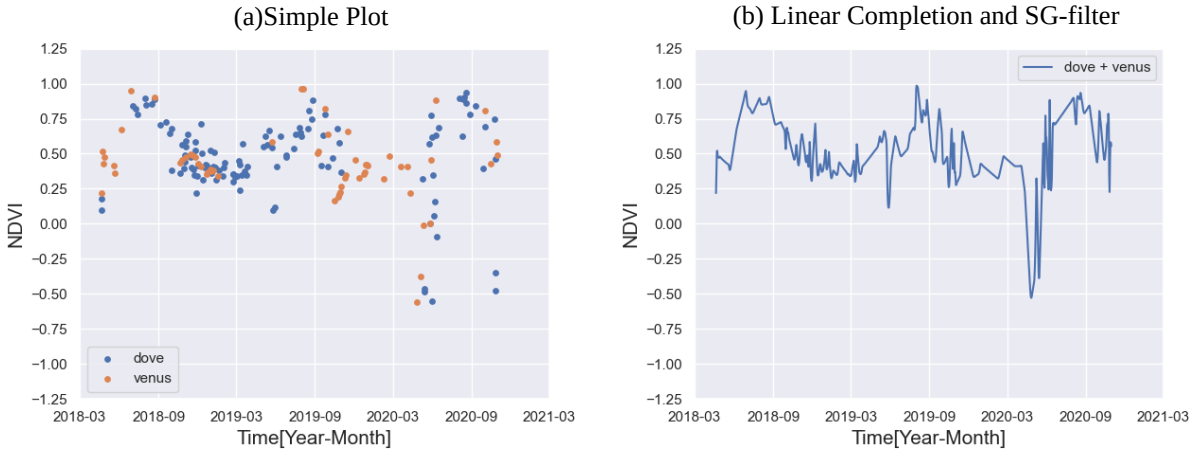

Fig. 4 Time-series NDVI at Farmland Pixel
(a)Simple Plot (b)After Linear Completion and SG-filter

4.3. Tracking Vegetation with Respect to Harvest Detection

The harvest date data of a total of 200 plots given by the two business corporations as the correct answer data for 2019 and 2020 are used to detect the harvest date. In addition to NDVI, we also tracked the time series of EVI2 to detect the harvest date. we computed the smoothed time series NDVI and EVI2 for each of the 200 plots at the center pixel. Again, to reduce noise, 3 x 3 pixels centered on the centroid pixel were averaged to make a representative value for each field.

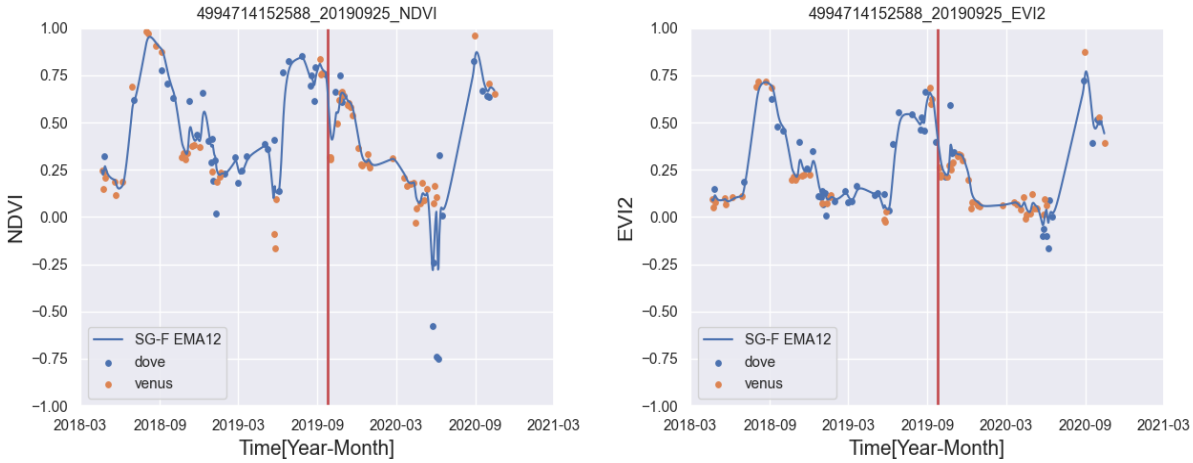

Fig. 5 Time series plot of NDVI and EVI2 in one crop field given a harvest date of 2019.

Fig. 5 shows the NDVI and EVI2 plots (blue for Dove, orange for VENμS), the graph of SG-f applied and EMA-12 applied, and the harvest date (red vertical line) for one crop field with 2019 harvest date data. Since there is still a large amount of fine variation in the data just after applying SG-F earlier, we further took the exponential moving average (EMA) of them with a window size of 12.

EVI2 shows less variance in the data over the entire period compared to the NDVI time series plot. In particular, we can see that the plots of May and June 2020, which had values around -0.75 in NDVI, are strongly suppressed in EVI2. As for the highest value of the indicator around September of each year, the NDVI shows the highest value in 2018, while the EVI2 shows the highest value in September of 2020, suppressing the value in 2018.

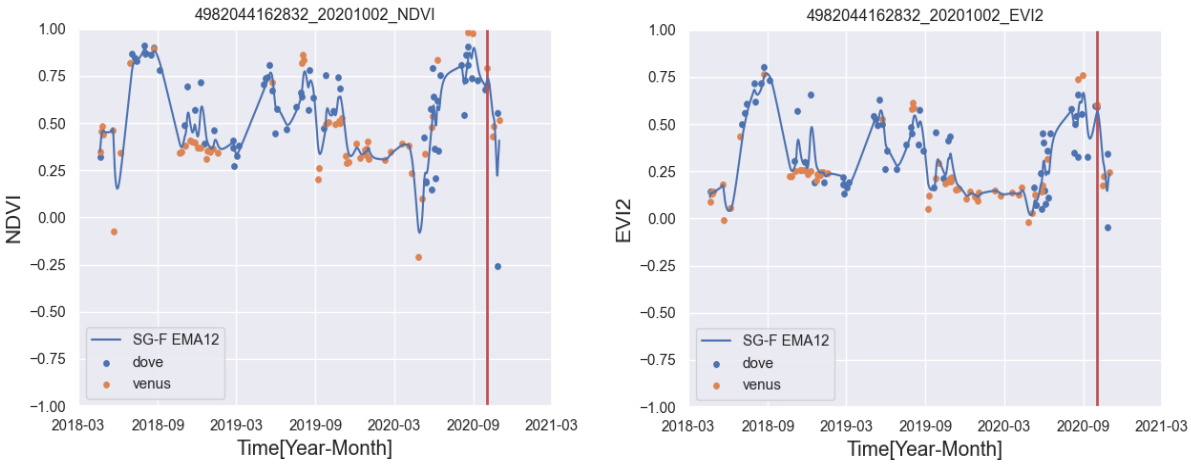

Fig. 6 Time series plot of NDVI and EVI2 in one crop field given a harvest date of 2020.

On the other hand, Fig. 6 shows the time series change and harvest date for one crop field with harvest data in 2020, which is different from the field in Fig. 5. Even in this case, the NDVI, which had a low value of about -0.25 around May 2020, is near 0 in EVI2, the same as the points before and after in the time series.

The time series of NDVI and EVI2 in 2019 and 2020 show that the values of each index decreased significantly around the harvesting date. In both 2019 and 2020, the values of NDVI decreased from around 0.8 to 0.5 before and after harvesting, while the values of EVI2 decreased from around 0.6 to 0.25 before and after harvesting. Although some previous studies have used Moving Average Convergence Divergence (MACD) to identify the end of cover crops (Gao, et al., 2020), it is considered to be useful to simply focus on the magnitude of the change when detecting a phenomenon such as harvesting, where a large change is observed before and after the event.

4.4. Harvest Detection

We hypothesized that a simple threshold-based method for NDVI values might be effective, based on a consideration of time series changes in some field data. We decided to predict the harvest date as the date when the NDVI value fell below 0.7 in the time series in September or October.

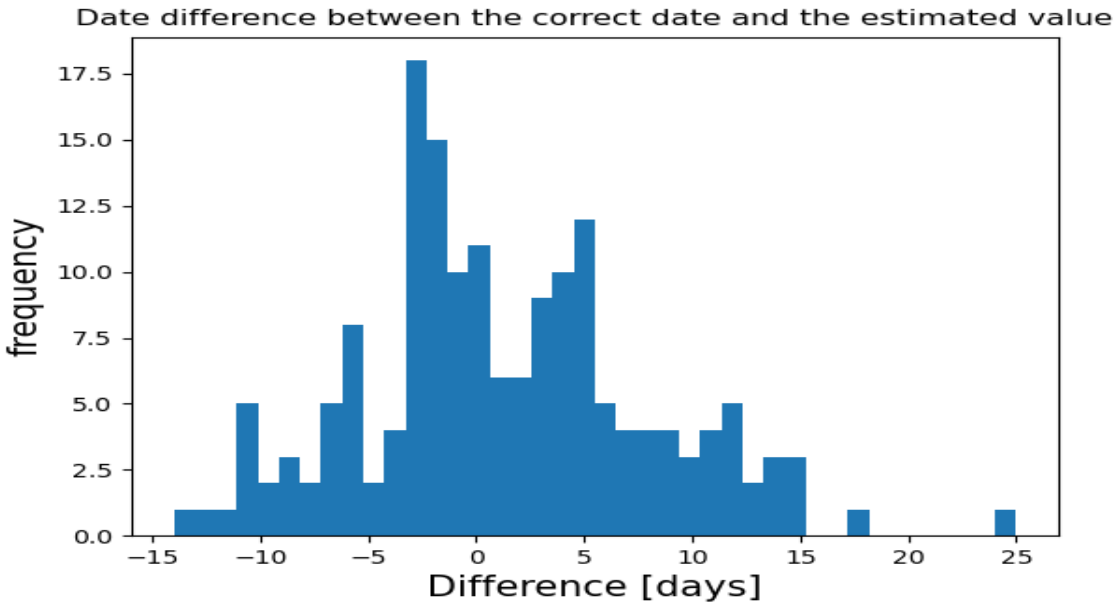

Fig. 7 Histogram of the difference between the predicted harvest date and the actual harvest date, which is predicted using NDVI

The results are shown in Fig. 7 and Table 2. Fig. 7 shows the histogram of the difference between the predicted and actual harvest dates for 200 crop field given the correct data. A positive value means that the predicted date was

before the actual harvest date. The absolute mean of the deviations was 5.4 days. While most of the prediction dates were within 10 days before or after the actual harvest date, there were two points with errors of 15 days or more.

Table. 2 Results for seeding and harvest detection

	Correct	Fail	Total	Accuracy
Area1 2020	12	8	20	60.0
Area 2 2019	61	15	76	**80.3**
Area 2 2020	70	34	104	67.3
Overall	143	57	200	71.5

Table. 2 shows the detail results. The data classified as "Correct" is when the forecast date was within 12 days before or after the actual harvest date. The accuracy for correct detection of harvest date was 71.5% (n = 200). The accuracy of the predictions for 2020 was lower than that for 2019. This may be due to the fact that less data was available in 2020 than in 2019 due to unseasonable weather around September.

A simple detection method with a short computation time was able to detect the harvesting date with an accuracy of more than 70%. On the other hand, compared to the previous studies, the results were not as good as the results of Shang's 90% and Sebastián's 94% (Shang, et al., 2020) (Sebastián, et at., 2021). The reason for this may be climatic factors such as the difficulty of obtaining optical satellite data in Japan due to rainfall during September and October, when harvesting tends to take place. In addition, there is still room for improvement in the harvesting method using the data obtained from the satellite images.

5. CONCLUSION

In this work, we first created a time-series data-cube to integrate Dove and VENμS satellites data after correcting image misalignment, excluding cloudy scene and so on. Next, we tracked the changes in reflectance over three years. A large scattering in reflectance was observed due to incomplete atmospheric correction and different observation geometry. These problems were greatly reduced by using NDVI as a band ratio to show the vegetation index. Moreover, it was found that under proper preprocessing, different satellite data can be treated equivalently as NDVI values. Furthermore, another vegetation index, EVI2, which was tracked at the same time as NDVI, showed a smaller variance than NDVI and a stronger ability to suppress outliers. Finally, a simple threshold-based method using time-series NDVI was used to detect harvesting at 200 sites, resulting in a prediction accuracy of over 70% and a prediction gap of 5.4 days. Although the time series tracking is affected by the local climate, there is room for further improvement in the harvest detection method.

6. REFERENCES

Adrian, V.R., Gaius, R.S., 2009. Advantages of a two band EVI calculated from solar and photosynthetically active radiation fluxes. Agricultural and Forest Meteorology, Volume 149, Issue 9, pp. 1560-1563, DOI: 10.1016/j.agrformet.2009.03.016.

Cai, Z., Jönsson, P., Jin, H., Eklundh, L., 2017. Performance of Smoothing Methods for Reconstructing NDVI Time-Series and Estimating Vegetation Phenology from MODIS Data. Remote Sensing, 9(12), pp. 1271. DOI: 10.3390/rs9121271.

Carlos, G.B., Karine, A., Xavier, B., 2021. Impact of the number of dates and their sampling on a NDVI time series reconstruction methodology to monitor urban trees with Venμs satellite. International Journal of Applied Earth Observation and Geoinformation, Volume 95, pp. 102257. DOI: 10.1016/j.jag.2020.102257

Compton, J.T., 1979. Red and photographic infrared linear combinations for monitoring vegetation. Remote Sensing of Environment, Volume 8, Issue 2, pp. 127-150, DOI: 10.1016/0034-4257(79)90013-0.

Feng G, Jeff, M., Matt, S., Forrest, H., 2006. On the blending of the Landsat and MODIS surface reflectance: predicting daily Landsat surface reflectance. IEEE Transactions on Geoscience and Remote Sensing, vol. 44, no. 8, pp. 2207-2218, DOI: 10.1109/TGRS.2006.872081.

Grabska, E., Hostert, P., Pflugmacher, D., Ostapowicz, K., 2019. Forest Stand Species Mapping Using the Sentinel-2 Time Series. Remote Sensing, 11(10), pp. 1197, DOI: 10.3390/rs11101197

Gao, F., Anderson, M., Daughtry, C., Johnson, D., 2018. Assessing the Variability of Corn and Soybean Yields in Central Iowa Using High Spatiotemporal Resolution Multi-Satellite Imagery. Remote Sensing, 10(9), pp. 1489. DOI: 10.3390/rs10091489.

Gao, F., Anderson, M.C., Hively, W.D., 2020. Detecting Cover Crop End-Of-Season Using VENμS and Sentinel-2 Satellite Imagery. Remote Sensing, 12(21), pp. 3524.

Hasi, B., Andrew, M., Wataru, T., Yoshiki, Y., 2020. Spatiotemporal analysis of deforestation in the Chapare region of Bolivia using LANDSAT images. Land Degradation & Development, Volume 31, Issue 18, pp. 3024-3039. DOI: 10.1002/ldr.3692.

Jin, C., Per. Jönsson, Masayuki, T., Zhihui, G., Bunkei M., Lars, E., 2004. A simple method for reconstructing a high-quality NDVI time-series data set based on the Savitzky–Golay filter. Remote Sensing of Environment, Volume 91, Issues 3–4, pp. 332-344. DOI: 10.1016/j.rse.2004.03.014.

Koichi, I., Takafumi, A., Hiroshi, N., Koji, K., Tatsuo, H., 2008. A Palmprint Recognition Algorithm Using Phase-Only Correlation. IEICE TRANS. FUNDAMENTALS, VOL.E91–A, NO.4, pp. 1023-1030

Manivasagam, V.S., Kaplan, G., Rozenstein, O., 2019. Developing Transformation Functions for VENμS and Sentinel-2 Surface Reflectance over Israel. Remote Sensing, 11(14), pp. 1710. DOI: 10.3390/rs11141710

Petersen, L.K., 2018. Real-Time Prediction of Crop Yields From MODIS Relative Vegetation Health: A Continent-Wide Analysis of Africa. Remote Sensing, 10(11), pp. 1726, DOI: 10.3390/rs10111726

Quan, W., Samuel, A., John, T., André, G., 2005. On the relationship of NDVI with leaf area index in a deciduous forest site. Remote Sensing of Environment, Volume 94, Issue 2, pp. 244-255, DOI: 10.1016/j.rse.2004.10.006.

Rao, Y., Zhu, X., Chen, J., Wang, J., 2015. An Improved Method for Producing High Spatial-Resolution NDVI Time Series Datasets with Multi-Temporal MODIS NDVI Data and Landsat TM/ETM+ Images. Remote Sensing, 7(6), pp. 7865-7891. DOI: 10.3390/rs70607865

Savitzky, A., Golay, M.J.E., 1964. Smoothing and differentiation of data by simplified least squares procedures. Analytical Chemistry, 36, pp. 1627-1639.

Sebastián, A., Néstor, C.D.L., Sebastián, B., Ayelen, P., Cecilia, C., María, C.P., 2021. Exploiting Sentinel-1 data time-series for crop classification and harvest date detection. International Journal of Remote Sensing, 42:19, pp. 7313-7331. DOI: 10.1080/01431161.2021.1957176.

Seng, H., 2013. A new approach of moving average method in time series analysis. Conference on New Media Studies (CoNMedia), pp. 1-4, DOI: 10.1109/CoNMedia.2013.6708545.

Shang, J., Liu, J., Poncos, V., Geng, X., Qian, B., Chen, Q., Dong, T., Macdonald, D., Martin, T., Kovacs, J., Walters, D., 2020. Detection of Crop Seeding and Harvest through Analysis of Time-Series Sentinel-1 Interferometric SAR Data. Remote Sensing, 12(10), pp. 1551. DOI: 10.3390/rs1210155.

Suming, J., Limin, Y., Zhe, Z., Collin, H., 2017. A land cover change detection and classification protocol for updating Alaska NLCD 2001 to 2011. Remote Sensing of Environment, Volume 195, pp. 44-55. DOI: 10.1016/j.rse.2017.04.021.

Zhangyan, J., Alfredo, R.H., Kamel, D., Tomoaki, 2008. M., Development of a two-band enhanced vegetation index without a blue band. Remote Sensing of Environment, Volume 112, Issue 10, pp. 3833-3845, DOI: 10.1016/j.rse.2008.06.006.

Zhe, Z., Junxue, Z., Zhiqiang, Y., Amal, H.A., Warren, B.C., Shi, Q., Congliang, Z., 2020. Continuous monitoring of land disturbance based on Landsat time series. Remote Sensing of Environment, Volume 238, pp. 111116, DOI: 10.1016/j.rse.2019.03.009.